A STUDY OF ATOMIC ORDERING IN III-V SEMICONDUCTORS

Undergraduate Thesis

Presented to the University Honors Program of the

University of North Texas in Partial

Fulfillment of the Requirements for the

University Honors Program

By

Ryan J. Cottier

Denton, Texas

August 2002

A STUDY OF ATOMIC ORDERING IN III-V SEMICONDUCTORS

Ryan James Cottier	Date

APPROVED:

Dr. Gloria Cox	Date
Dr. Chris Littler	Date

TABLE OF CONTENTS

LIST OF ILLUSTRATIONS

LIST OF TABLES

CHAPTER I

INTRODUCTION

The overwhelming majority of the semiconductor industry is based on research and production of silicon-based materials. Si bipolar devices have maintained the requirements dictated for high-speed, high-current, and low-noise devices [1]. Despite the underlying push to maintain Si as the primary technological material, Si poses some major limitations. The Si band structure displays an indirect energy gap between the valence and conduction bands. Therefore, electron excitation or recombination across this indirect gap requires a two-step process involving both a phonon and photon. The complication of this route causes the electron to move along simpler, non-radiative routes, rendering all known Si-based devices optically inactive.

Due to these limitations, novel material systems which display a direct energy gap are required for the creation of all opto-electronic devices. GaAs and GaSb semiconductors have direct energy gaps of 1.4 and 0.7 eV respectively. They, as well as other III-V materials, have been the answer to the technological need for materials, which optically operate in the 1.3-1.5 μm wavelength range. The $GaAs_{1-x}Sb_x$ alloy system also exhibits a large bowing parameter, which can be exploited to engineer specific energy gap values.

In this undergraduate thesis, I will present a study of the $GaAs_{1-x}Sb_x$ alloy system. $GaAs_{1-x}Sb_x$ epilayers ($0.19 < x < 0.67$) were grown by molecular beam epitaxy on GaAs substrates with orientations of (001), (001)-8° toward (111)A, (001)-8° toward (111)B, (115)A, and (115)B. These orientations were chosen to encourage various degrees of CuPt-B type atomic ordering which is expected to reduce the fundamental energy gap significantly.

This document is organized into the following chapters: Chapter 2, which will discuss an overview of semiconductors and band structure, the temperature-induced variation of the band structure, the atomic structure of III-V materials, and atomic ordering and its effect on band structure; Chapter 3, which discusses the experimental techniques used including molecular beam epitaxy, Fourier transform infrared spectroscopy, and Hall effect; and Chapter 4, which will give the results and discussions of the experiments.

CHAPTER II

OVERVIEW

The discovery and application of semiconducting devices have revolutionized the civilized nations as we know them today. Over the past 80 years, scientists have delved into the complex workings of semiconductors due to the overwhelming flood of possible applications, including those we have yet to realize. In the late 1940s, the transistor,a simple semiconducting device which outputs different results depending on the conditions of the three inputs, was invented. The transistor led to the development of a computational machine, a device with almost unlimited capabilities. Continuing with the trend of the natural course of history, it is just as important today to understand semiconductors more and more completely.

2.1 Semiconductor Band Structure

It is beneficial to understand the nature of a bulk material's band structure, the energy $\varepsilon(k)$ of the electron states as a function of the wave vector k, in order to develop technologically useful semiconducting materials. Several optical and electronic properties can be understood by careful study of the band structure. The origin and significance of band structure can be understood by first considering the energy spectrum for a single atom, then a molecule, and finally a solid.

The wave function of the electrons in an isolated atom can be determined by solving the Schroedinger equation:

$$H\Psi = E\Psi$$

where H is the Hamiltonian operator. A fundamental outcome of quantum mechanics is that the wave solutions of this equation produces eigenvalues, E_n, which correspond to values of a discrete energy spectrum unlike the continuous energy spectrum which almost always results from classically computed mechanics. Due to the discrete nature of the solutions, the electrons themselves can only exist with specific values of energies, meaning their possible energies are quantized. For instance, the lithium atom, separated from any outside influence, will have its first three states, in order of increasing energy, labeled 1s, 2s, and 2p, where the numbers specify the particular quantum state and the letters specify the specific angular momentum state. The illustration of these states in Figure 1 (a) shows the ladder type arrangement resulting from this outcome [2].

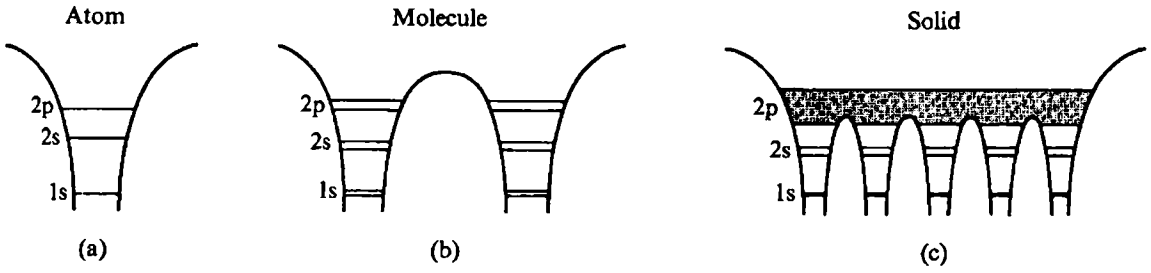

Figure 1. The evolution of the energy spectrum of Li from an atom (a), to a molecule (b), to a solid (c) [2].

According to quantum mechanics and the Pauli exclusion principle, no two electron can be in the same state. Quantum states can be further specified by another property, labeled spin, of which there are only two choices, spin up and spin down. Therefore, at most, two electrons can be in the 1s state as long as their spins are opposite. The same is true for 2s, 2p, and all other possible states. The lithium atom has three electrons, which are, at low temperatures, distributed as the following: two in the 1s state and one in the 2s state.

In creating the Li_2 molecule, the lithium atoms, initially at a distance allowing no interaction, are slowly brought together. As the individual atoms begin to interact, the energy states split into doublets of similar but slightly different energy, as shown in Figure 2 (b). The states split further as bonding with other Li atoms occurs. As the number of atoms increases to $\sim 10^{23}$, roughly the number of atoms in a macroscopic solid, shown in Figure 2 (c), the quantum states split so many times that the difference in energy between consecutive split levels is small enough to consider the energy continuous within that level. These energy states then make up a series of energy bands which are each separated by a gap. Using similar quantum mechanical calculations, one can determine a bulk material's band structure, the energy, $\varepsilon(k)$, of the electron states as a function of the wave vector, k.

The electrical nature of a material is directly associated with the calculated band structure. Conducting materials allow electrical current to flow freely when an electric field is applied. An insulator, however, strongly resists any electric current. It follows from band structure calcultions that this results from how full particular bands are. The requirement for electron flow is simply that an empty state exists and is accessible by a previously bound electron so that the electron may enter that new state. In a metal, shown in Figure 2 (a), one band of electronic states is only partially full of electrons; therefore, it takes only an infinitesimal increase in energy for the most energetic electrons to enter new states, and therefore move freely throughout the solid. In an insulator, shown in Figure 2 (b), one band, called the valence band, is completely filled with electrons, while the band above it in energy, the conduction band, is completely empty. The difference in energy between the top of the valence band and the bottom of the conduction band, the fundamental energy gap, is too large for electrons to jump across easily. A semiconductor, shown in Figure 2 (c), is similar to an insulator in that its valence band is completely full and the

conduction band is completely empty. However, the fundamental energy gap is of the order of 1 electron volt, small enough to allow some electrons to be thermally excited to the conduction band. Since both the valence and conduction bands then are only partially full, they become conducting.

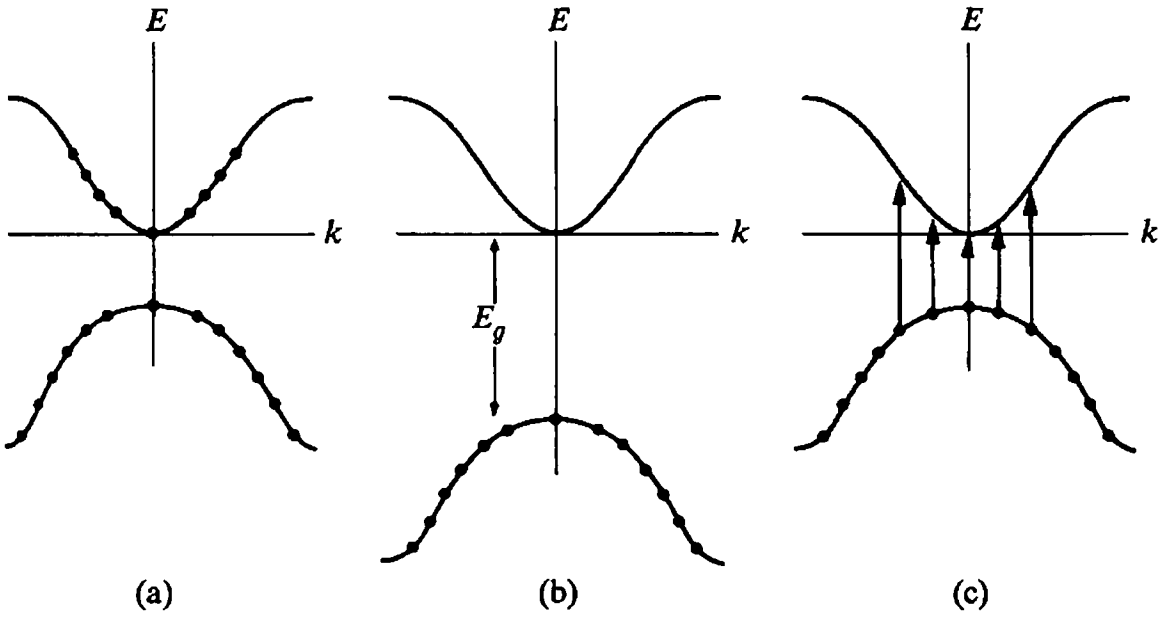

Figure 2. The distribution of electrons in the bands of (a) a metal, (b) an insulator, and (c) a semiconductor [2].

For semiconductors, the dispersion law can be calculated be assuming a parabolic band for the conduction and valence bands. If the top of the valence band and the bottom of the conduction band are at the same point in k-space, the energy gap is labeled direct, shown in Figure 3, and if they are at different points the gap is labeled indirect. If the energy of the conduction band bottom is taken as zero ($\varepsilon_c(k) = 0$), then the dispersion law of the bands in the vicinity of the Γ point ($k = (0,0,0)$) can be described by the Kane model [3] for the energy band structure.

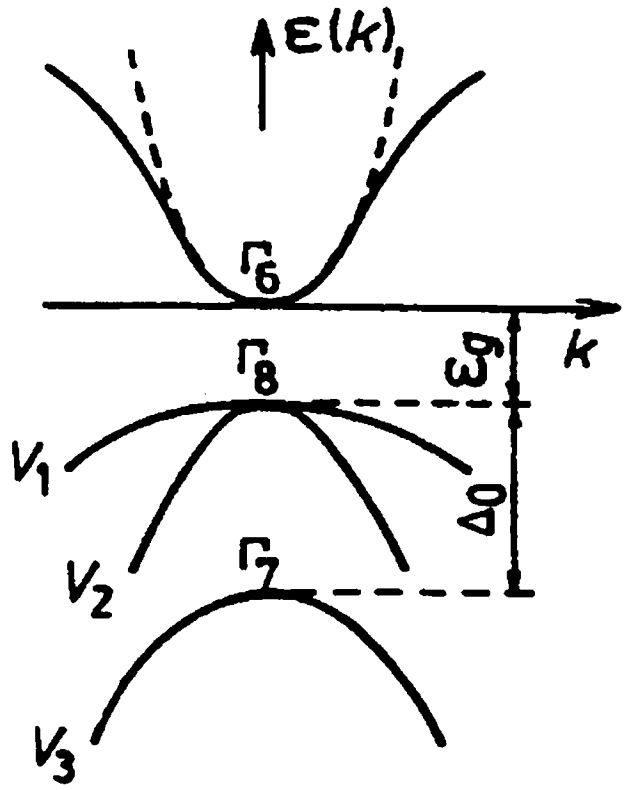

Figure 3. A model of the conduction and valence band edges for a typical III-V semiconductor [4].

2.2 Semiconductor Alloys

When growing and characterizing semiconducting materials, it is important to choose a material system which can allow for modification of deterministic properties such as energy gap and lattice constant. The use of alloyed systems, III-V systems for instance, is ideal for this particular purpose.

The simplest III-V compounds include just one element each from Group III and Group V of the periodic table; two examples are GaAs and GaSb which have bandgaps of about 1.4 eV and 0.7 eV respectively. Since these binaries are of specific lattice spacing, 5.6 and 6.1 Å

respectively, epitaxial growth on substrates, which are of dissimilar lattice constant, often results in strain defects. The combination of two binary alloys, AB and AC, where A represents a Group III element and B and C represent Group V elements, can create a ternary alloy, AB_xC_{1-x}, where x is the fraction of Group V spaces occupied by B. Addition of the element C the binary AB alters the lattice constant linearly proportional to x. Alteration of the lattice constant changes the energy gap, E_g, as seen in Figure 1, where the bowed lines represent the ternary compounds. This phenomenon allows not only for lattice matching to the substrate, but also bandgap engineering to create technologically useful bandgap values.

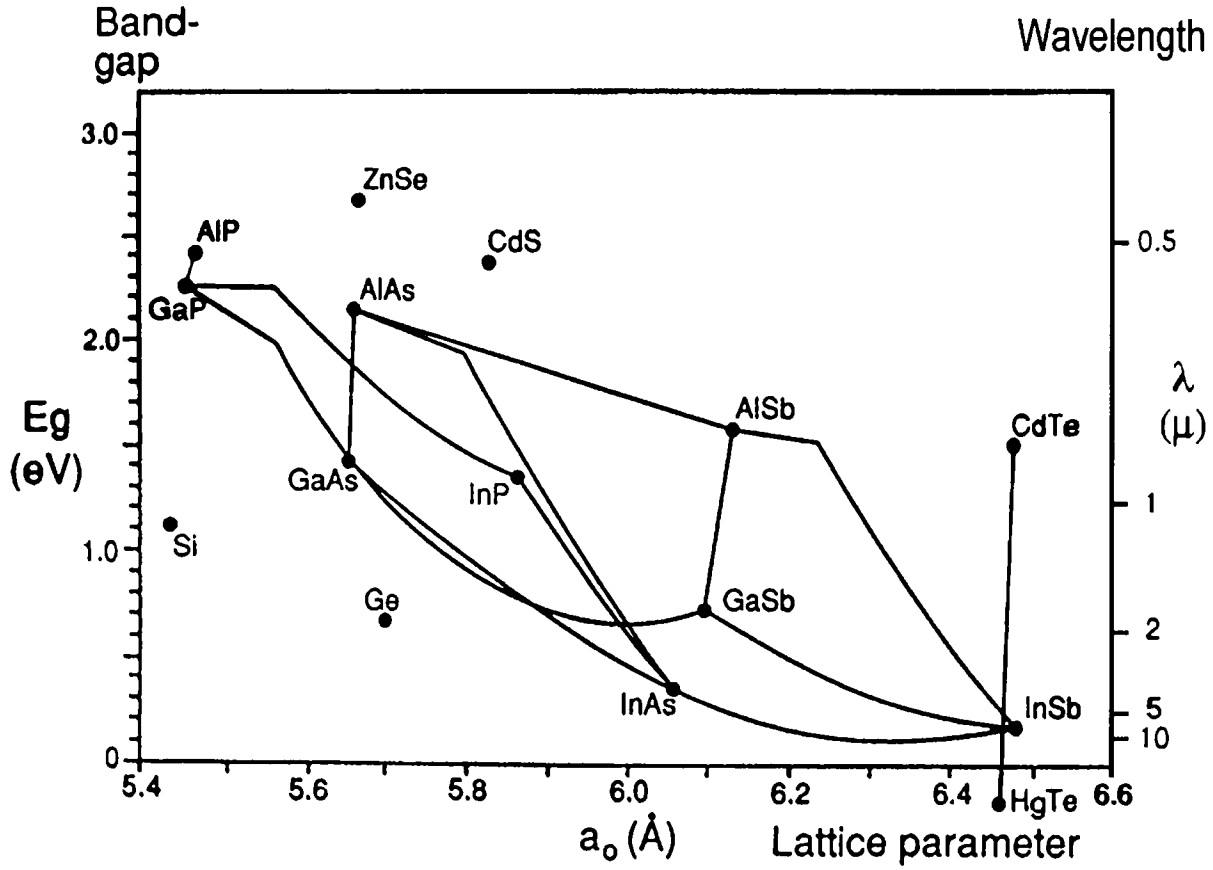

Figure 4. Variation of lattice constant and energy gap with composition for a number of semiconductors.

2.3 Temperature Dependence of Bandstructure

The energy gap value for III-V semiconductors is altered by a change in temperature. This is mainly due to the sum effects of electron-phonon interaction and thermal expansion. The former one is the more significant of the two and contributes greatly to the energy gap shift [5]. Several models have been put forth to describe the energy shift.

Varshni developed the following equation to describe the temperature dependence of the energy gap:

$$E_g(T) = E_g(0) - \frac{\alpha T^2}{\beta + T}$$

where $E_g(0)$ is the mean energy gap at 0 K, and α and β are the Varshni coefficients [6].

O'Donnell and Chen [7] have altered the Varshni semi-empirical equation into the following thermodynamic expression:

$$E_g(T) = E_g(0) - S\langle\hbar\omega\rangle\left[\coth\left(\langle\hbar\omega\rangle/2kT\right) - 1\right]$$

where S is a dimensionless constant and $\langle\hbar\omega\rangle$ is the average phonon energy.

Pässler and Oelgart [8] proposed the final model considered in this paper, which describes the temperature dependence of the energy gap in a different way:

$$E_g(T) = E_g(0) - \frac{\alpha\Theta}{2}\left(\sqrt[p]{1 + \left(\frac{2T}{\Theta}\right)^p} - 1\right)$$

where $\alpha = S(\infty) = -\left(dE(T)/dT\right)_{T\to\infty}$ is equal to the high temperature limiting value of the associated entropy, Θ is the characteristic phonon temperature that represents the effective phonon energy, and p is an empirical parameter related to the shape of the electron-phonon spectral function [9, 10].

2.4 Zinc Blende

Crystal structure refers to the spatial arrangement of atoms within a solid. The structure of a crystal has very deterministic effects on the materials band structure. One commonly occurring semiconductor crystal structure is the zinc blende, shown in Figure 4, so called because of its occurrence in materials like ZnS and ZnSe. Zinc blende resembles the diamond structure because both consist of two face centered cubic (fcc) lattices offset by the vector $a\left(\frac{1}{4},\frac{1}{4},\frac{1}{4}\right)$,

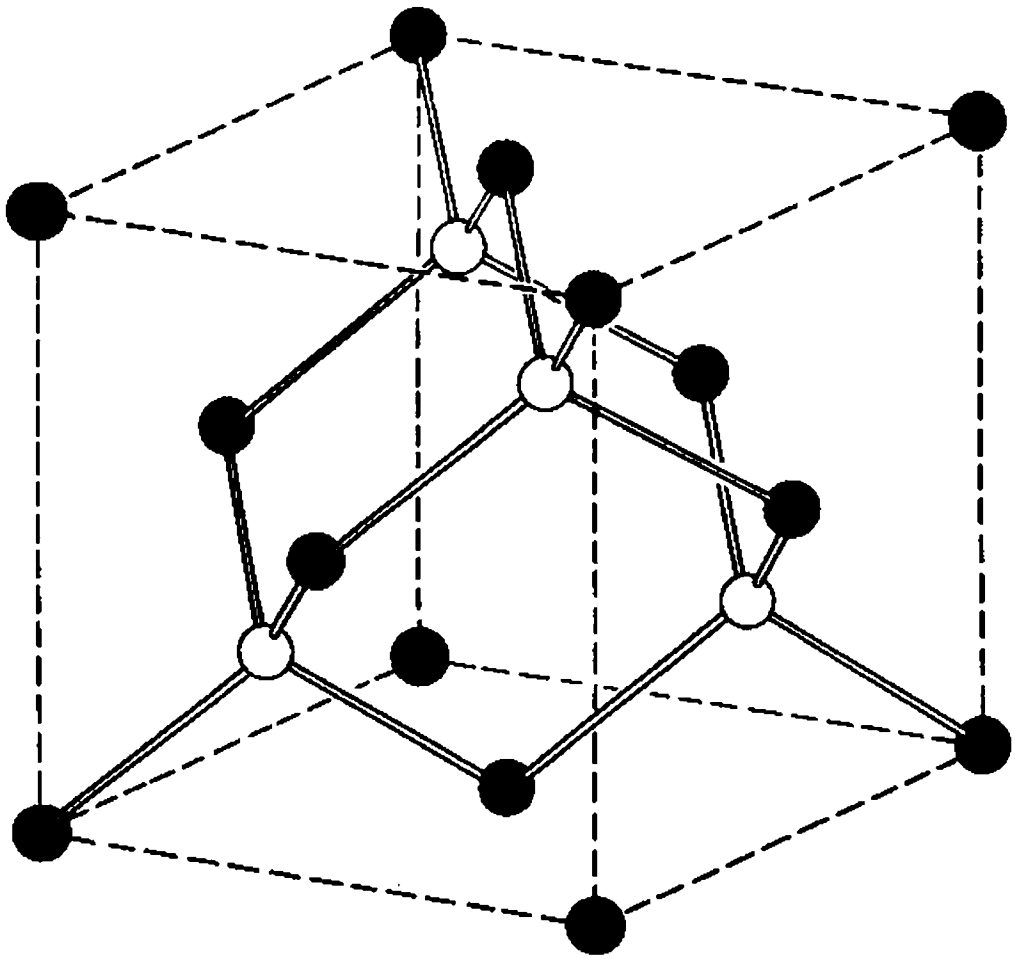

Figure 5. Crystal structure of cubic zinc sulfide (zinc blende) [11].

where a is the cubic lattice spacing. In diamond, a carbon atom occupies every lattice site, whereas in zinc blende, the two fcc lattices are occupied with different types of elements. III-V compounds form with this crystal structure, where all Group III elements rest on one fcc lattice and all Group V elements on the other.

2.5 Atomic Ordering

During the growth of a zinc blende semiconductor, there are two types of positions for the individual atoms to situate, on one of the two fcc lattices. The Group III atoms exclusively fill one fcc lattice while the Group V atoms exclusively fill the other. It originally was expected that, while growing a ternary or quaternary alloy, the group III (or V) atoms will distribute themselves randomly over their exclusive fcc lattice. This seems likely since each lattice point is exactly alike, and therefore there are no preferential points.

However, certain growth conditions can result in temporarily unequal lattice points, therefore de-randomizing the growth process. CuPt-B type ordering occurs due to surface reconstruction during growth [12]. In molecular beam epitaxy of $GaAs_{1-x}Sb_x$, the group V surface atoms (As and Sb) each have two dangling bonds which lower their energy by dimerizing, or forming bonds with another Group V atom. This tends to decrease the lattice spacing between subsurface atoms directly below the dimers while increasing the spacing between atoms not below dimers. The smaller lattice spacing tends to attract the smaller of the group V atoms, As, while the larger lattice spacing attracts Sb. This temporarily breaks the symmetry, decreases the randomness, and freezes in the ordering as subsequent layers are grown. It happens that the naturally occurring order consists of ordered Group V planes in the (111)B direction, and, for perfect ordering (which can only happen for x=0.5), layers in the (111)B

direction alternate between layers which contain completely As and layers which contain completely Sb [12]. This is called CuPt-B ordering and is shown in Figure 6.

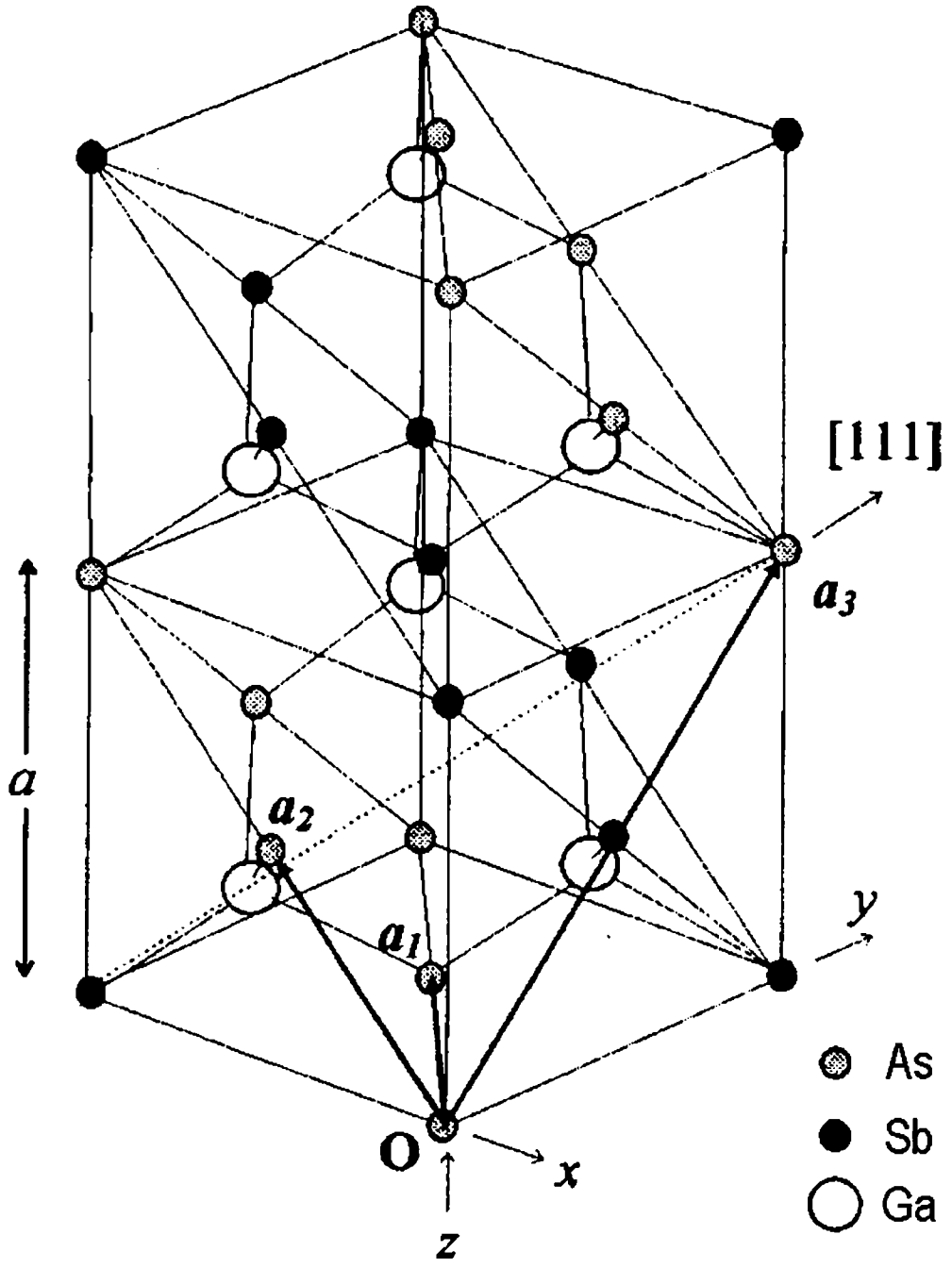

Figure 6. The crystal structure of a completely CuPt-Ordered $GaAs_{0.5}Sb_{0.5}$. The primitive Bravais lattice vectors are a_1, a_2, and a_3 [13].

CuPt type ordering is predicted to have significant effects on the optical and electrical properties of the layers [12]. Wei and Zunger [14,15] proposed the following theoretical formula to describe the energy gap reduction resulting from the CuPt-B ordering within the alloy system:

$$\Delta E_g(S) = E_g(S) - E_g(0) = \Delta E_g(1) \cdot S^2$$

where S is called the ordering parameter and $S = 0$ for complete randomness and $S = 1$ for perfect ordering.

CHAPTER III

EXPERIMENTAL TECHNIQUES

3.1 Molecular Beam Epitaxy

3.1.1 Concept

Molecular beam epitaxy (MBE) is the growth of epitaxial thin films on a heated substrate using thermal energy beams of atoms or molecules in an ultra-high vacuum environment. MBE has advantages over more developed growth methods like liquid phase epitaxy and vapor phase epitaxy because the film thickness can be more precisely controlled due to slower layer growth. Further, MBE growth is achieved at much lower temperatures (500-600°C for GaAs), which is low enough not to disturb abrupt compositional or doping profiles because of negligible bulk diffusion. MBE growth also allows the ability for *in situ* analysis using reflection high-energy electron diffraction (RHEED) to monitor growth rate and composition.

The basic elements used in an MBE setup are shown in Figure 7. The effusion cells contain high purity materials, which are heated to the evaporation temperature for that particular material. This creates an atomic or molecular flux which can be turned on or off by the electrical control of a shutter. The beams are incident on a substrate (GaAs wafer shown in figure), which is mounted on a molybdenum heating block. The temperature chosen for the heating block depends on what type of films are being grown on what type of substrate. Generally, the temperature is slightly below whatever temperature the material being grown becomes unstable. The substrate is rotated about the axis parallel to

the growth direction allowing for uniform growth and discouraging phase separation. The entire process takes place in a UHV chamber with a background pressure of $\sim 10^{-10}$ torr.

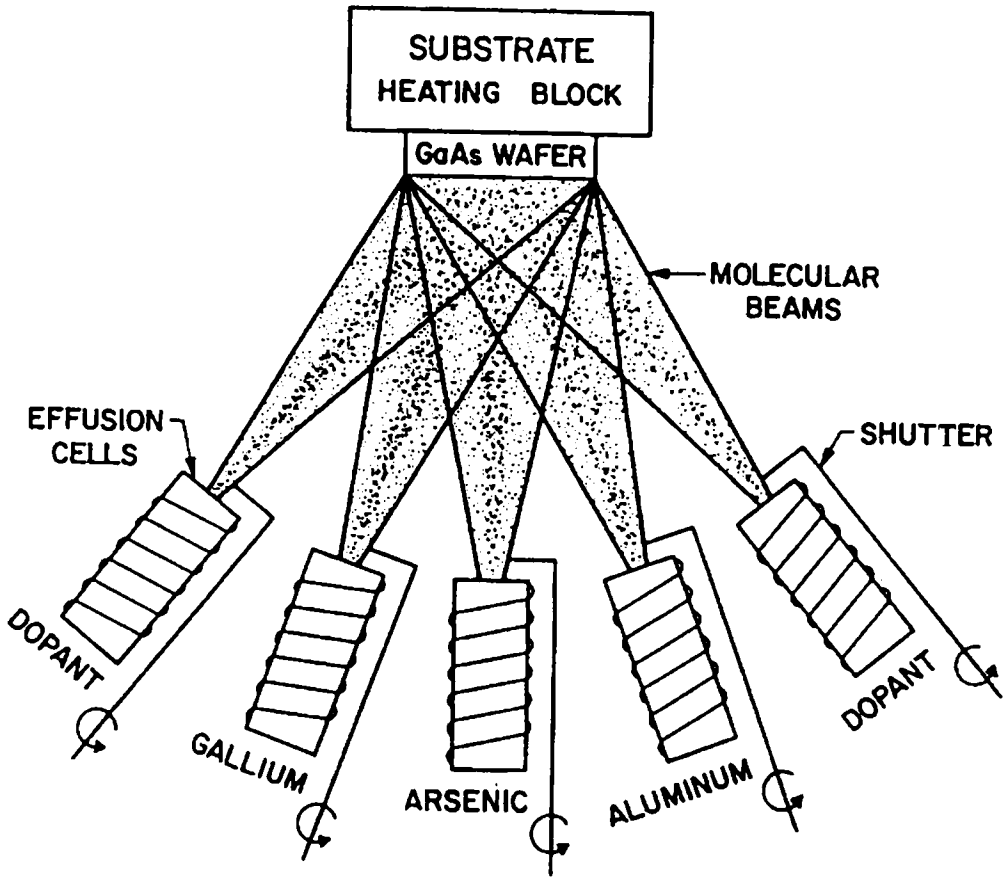

Figure 7. Basic evaporation process during MBE [16].

3.1.2 Experimental Setup

$GaAs_{1-x}Sb_x$ films, $0.19<x<0.77$, were grown by MBE on GaAs substrates with orientations of (001), (001)-8° toward (111)A, (113)A, (113)B, and (115)B with the knowledge that these growth parameters would produce samples which were CuPt-B ordered with varying degrees of order parameter. The MBE chamber used was similar to

the system shown in Figure 8, which consists of a growth chamber, a vacuum interlocked degassing chamber, and an introduction chamber.

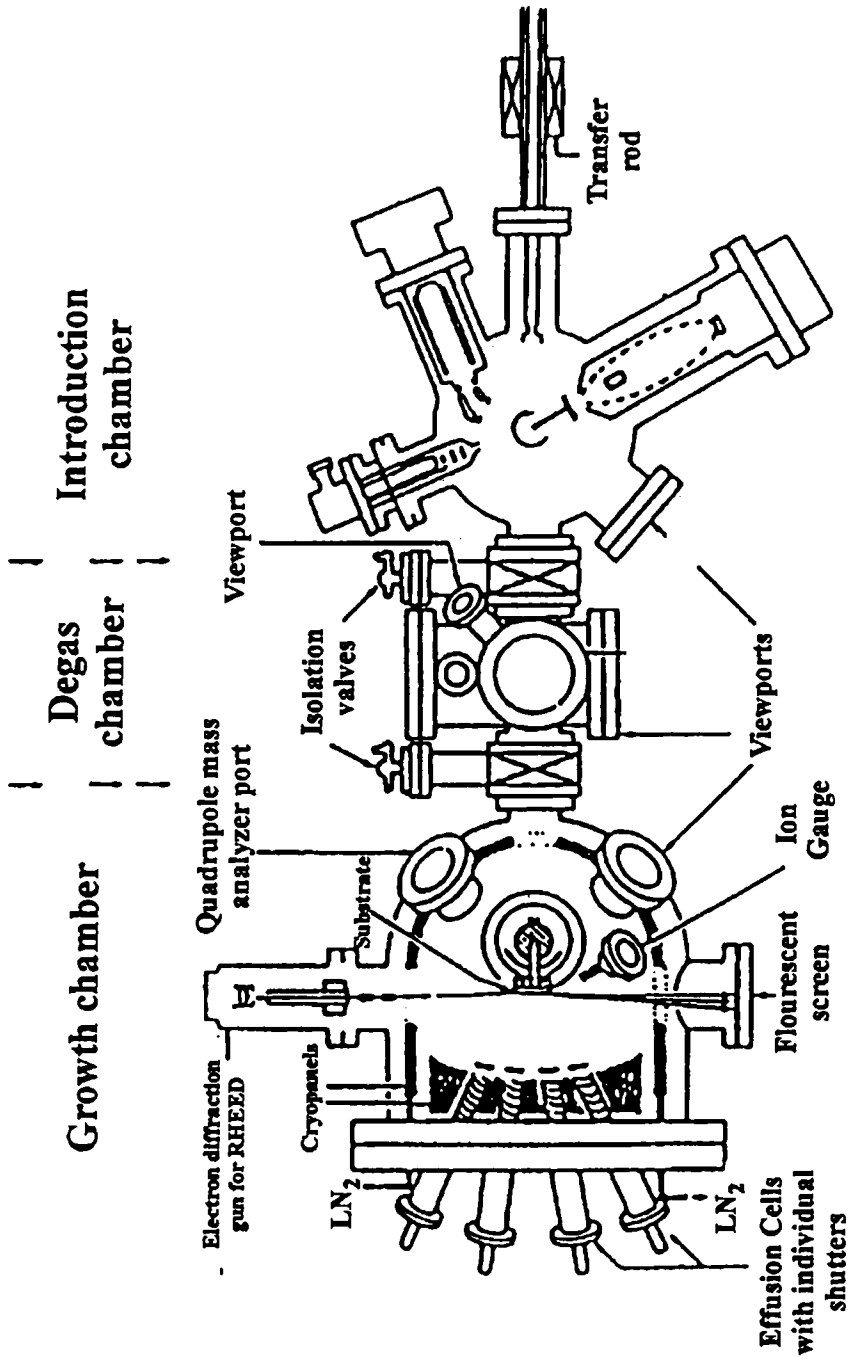

Figure 8. Schematic cross section of a UHV system for MBE growth and surface analysis chamber [16].

The system is first vacuum pumped by a turbo pump and rotary pump in series to a pressure of 10^{-8} Torr, and then it is pumped by ion pumps to a background pressure of 10^{-10} Torr. Further, the growth chamber has a system of liquid nitrogen distributing capillaries, which cool the chamber walls reducing contamination caused by out-gassing during growth. The substrate heater was maintained at either 525°C or 625°C for different samples. The growth rate was monitored by RHEED patterns on a phosphor screen. The Knudsen cells (effusion cells) were mounted on a vertical flange and were arranged radially and aimed at the substrate. The cells were heated by individual resistance heaters, and the growth was controlled by programmable shutters. The partial pressures, determined by mass spectroscopy, of the arsenic and antimony fluxes were on the order of 10^{-5} and 10^{-7} Torr respectively. The crystalline quality of the samples and their compositions were determined by double crystal X-ray diffraction.

The Table 1 gives the details of the samples grown:

Sample	Substrate Orientation	Composition (x)	Growth Temperature (°C)
a	(001)	0.19	625
b	(115)B	0.53	525
c	(001) 8°→(111)B	0.57	525
d	(001) 8°→(111)A	0.65	525
e	(001)	0.67	525

Table 1. Sample details.

3.2 Fourier Transform Infrared Spectroscopy

3.2.1 Concept

Several methods of characterizing semiconductors involve observing the way particular materials absorb light. The most important absorption process involves the transition of electrons from the valence to the conduction band [2]. This process is referred to as fundamental absorption. For fundamental absorption to occur, an incident photon must be greater than or equal in energy to the fundamental energy gap. This causes transitions similar to those shown in Figure 9. The center transition represents an electron being excited by a photon of energy equal to E_g, and while the other transitions represent transitions cause by photons of energy greater than E_g. From quantum perturbation theory

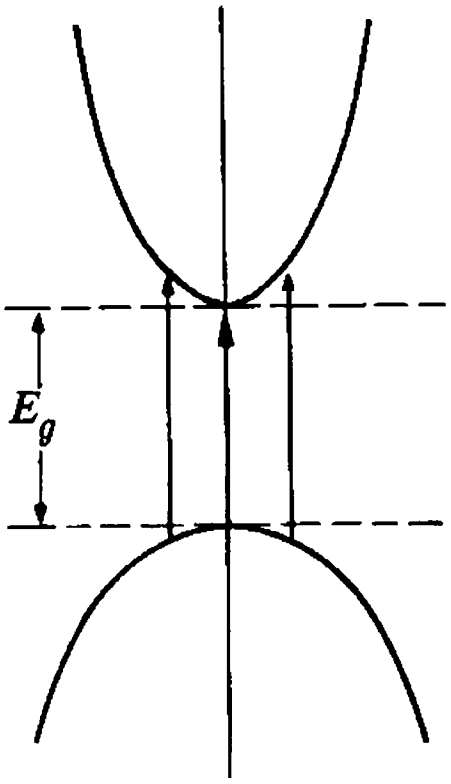

Figure 9. The fundamental absorption process in semiconductors [2].

it is found that the absorption coefficient, k, can be represented as:

$$k \propto (h\nu - E_g)^{1/2}$$

where ν is the frequency of the incident light [2]. The energy gap, E_g, can be determined by analysis of the absorption spectra.

Fourier transform infrared spectroscopy uses a light source from which specific frequencies of light can be extracted. These specific frequencies are incident on a sample, and the absorbance is calculated based on the intensity of the transmitted light.

3.2.2 Experimental Setup

$GaAs_{1-x}Sb_x$ samples were studied using absorption techniques. Our absorption studies were carried out on a Nicolet Nexus 470 Fourier Transform Infrared (FTIR) Spectrophotometer (shown in Figure 10) over the energy range of 0.2 eV to 1.4 eV. A 300 W tungsten filament was used as a near infrared light source, and the transmitted light was collected by a mercury cadmium telluride detector. The samples were mounted on a liquid helium cooled cryostat shown in Figure 11 and aligned at normal incidence to the beam.

The experiment was computer software controlled. We first collected a background spectrum, which was the absorbance for a GaAs wafer mounted in the cryostat. This spectrum was subtracted from all our data spectra. The data was obtained for temperatures of 4 to 300 K, which was sustained by liquid helium cooling and a Lake Shore Cyrotronics temperature controller.

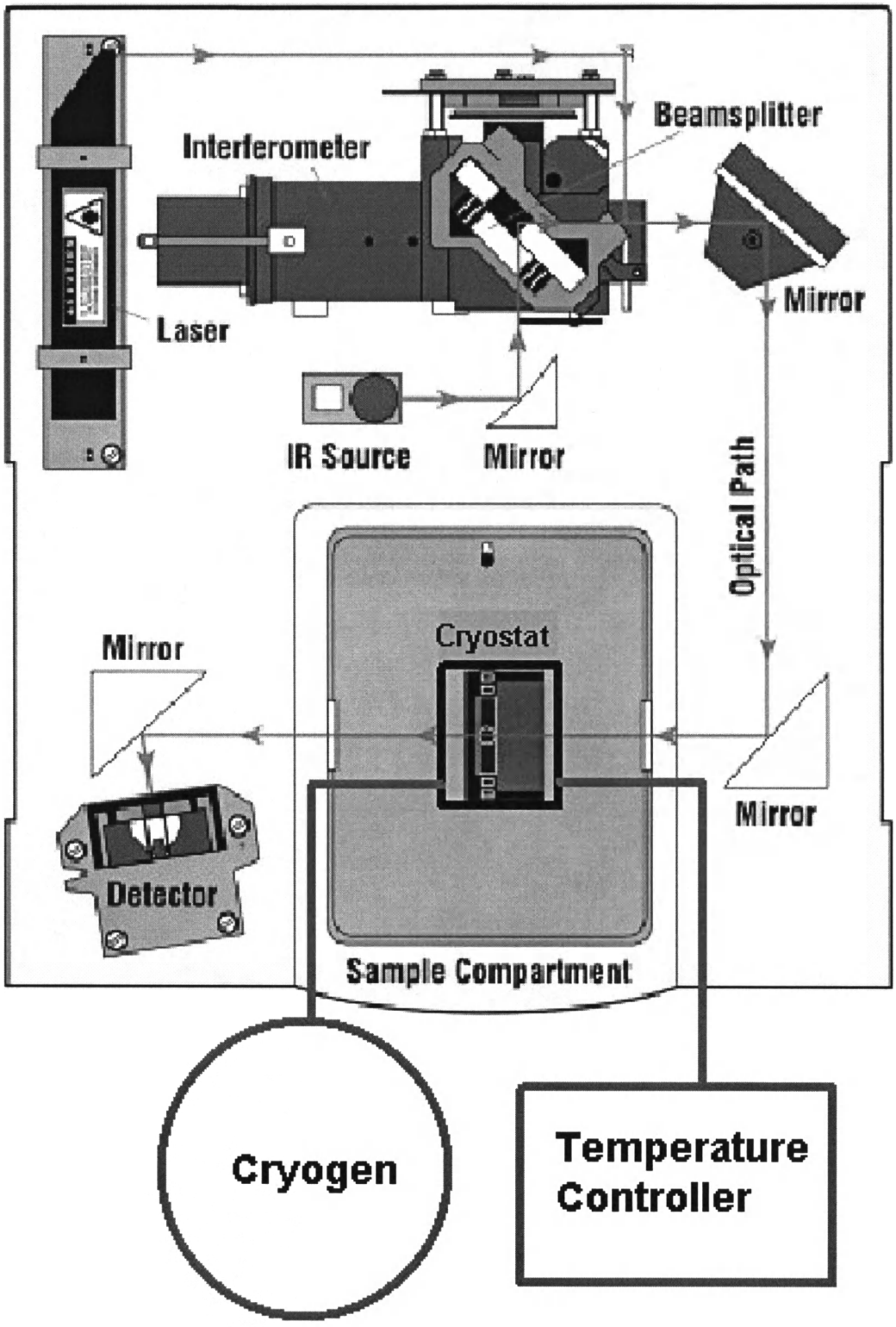

Figure 10. Nicolet Nexus 470 FTIR Setup.

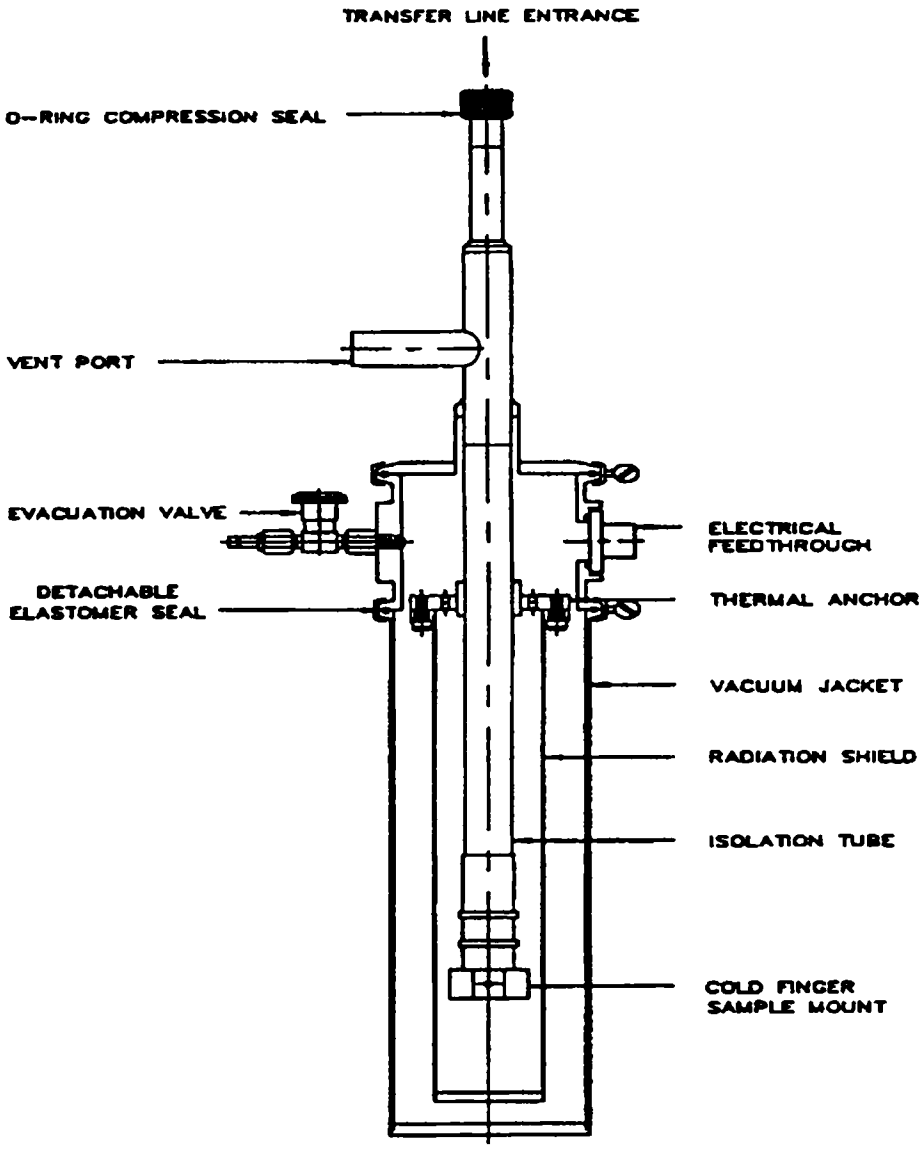

Figure 11. Janis Supervaritemp cryostat.

3.3 Hall Effect and Mobility

3.3.1 Concept

The Hall Effect experiment exploits the phenomenon that when a current passes through a sample perpendicular a magnetic field, a voltage is induced which is

perpendicular to both the current and the magnetic field. This results from the Lorentz force, $F_m = -e(\vec{v} \times \vec{B})$, which is exerted on electrons of charge $-e$ and velocity $\vec{v}$ in a magnetic field, $\vec{B}$. The deflected electrons (negative charge) accumulate at one boundary of the sample while the holes (positive charge) left behind accumulate on another boundary. This separation of charge results in a Hall field, ε_H, which counterbalances the Lorentz force. This is illustrated in Figure 12.

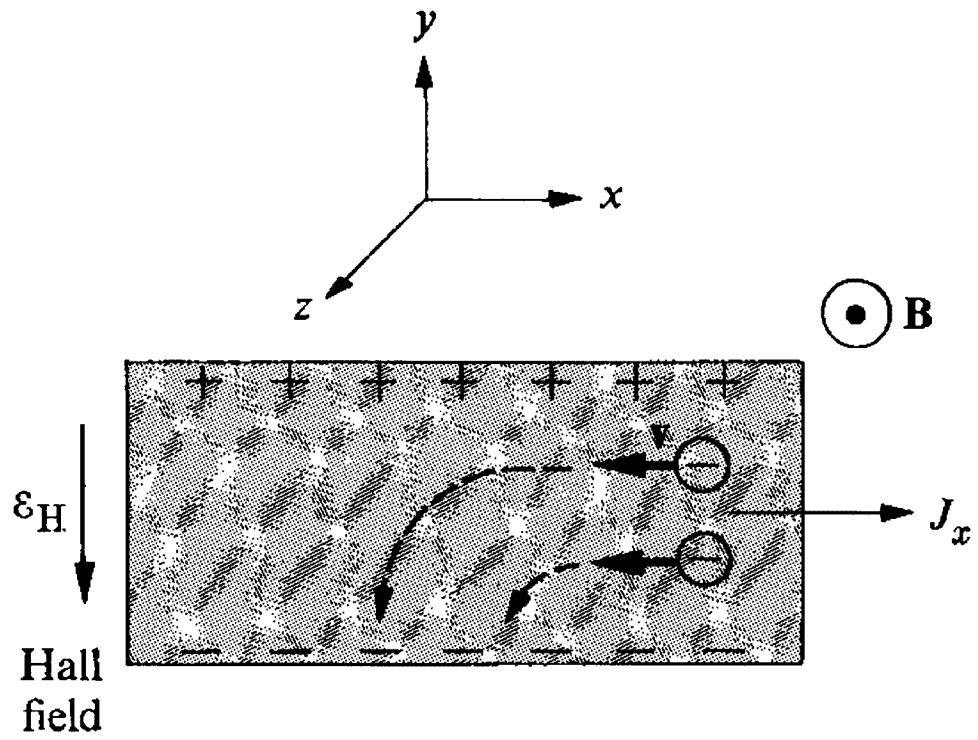

Figure 12. Origin of the Hall field and Hall effect [2].

In the diagram, F_m acts in the negative y-direction and has the value

$$F_m = ev_x B$$

Since the $F_H = F_m$, where $F_H = -e\varepsilon_H$ is the Hall force, then it follows that

$$\varepsilon_H = v_x B$$

In terms of measurable quantities, using $J_x = N(-e)v_x$ as the current density where N is the number of carriers and v_x is the velocity of the carriers,

$$\varepsilon_H = -\frac{1}{Ne} J_x B$$

and the Hall coefficient is taken as

$$R_H = -\frac{1}{Ne}$$

so that

$$\varepsilon_H = R_H J_x B$$

Further, the electron drift velocity is related to the applied electric field by the equation

$$\vec{v}_{drift} = \mu_d \vec{E}$$

where μ_d is the drift carrier mobility which is defined from

$$\vec{J} = \mu_c nq\vec{E}$$

where, in principle, μ_d is the same as μ_c, the conductivity mobility, n is the carrier concentration, and q is the charge of the carrier. The resistivity, ρ, is defined as

$$\rho = \frac{1}{\mu_c nq}$$

The mobility can be expressed I terms of the Hall coefficient and the resistivity as

$$\mu = |R_H|\frac{1}{\rho} = |R_H|\sigma$$

If, in Figure 13, terminal one is considered positive polarity for the current, I^+, and the direction of the magnetic field as shown is considered positive, B^+, then the Hall voltage, when

measured between terminals 3 and 4, will read negative at terminal 3 for negative charge carriers, n-type material, and positive for positive charge carriers, p-type material. The contacts placed on the rectangular sample should ideally be placed so that $V_H = 0$ in the absence of magnetic field. This does not occur since contacts have some amount of misalignment. First measuring the value and then measuring again under a reversed magnetic field can eliminate the misalignment potential.

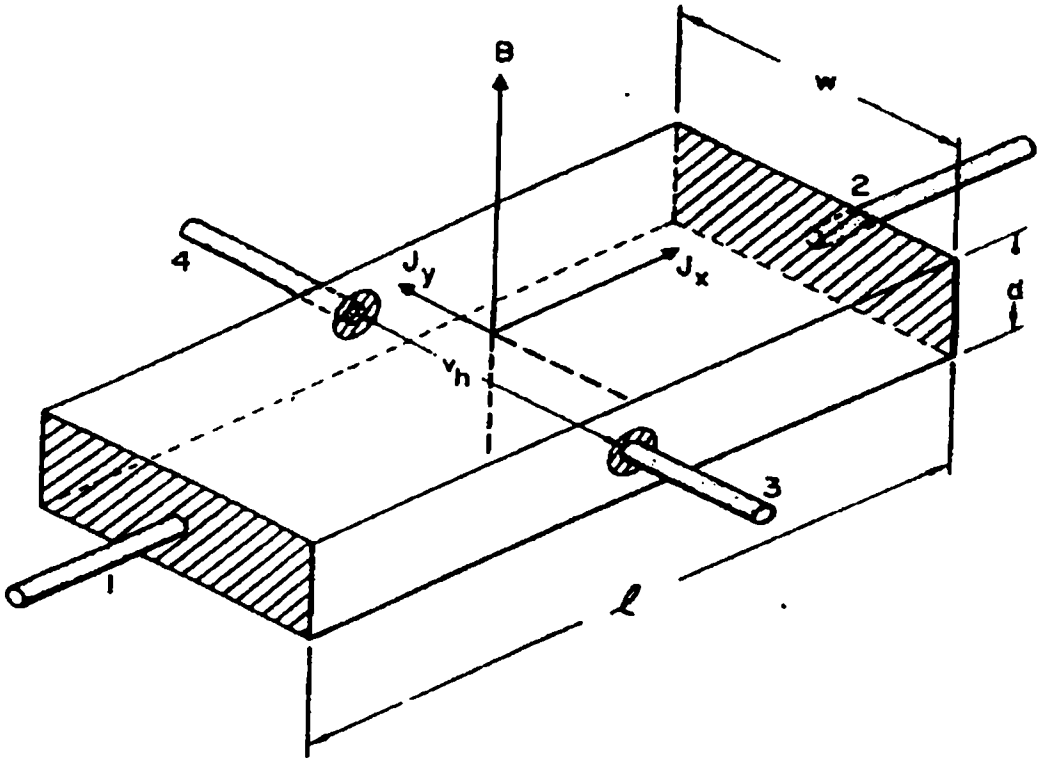

Figure 13. Schematic of a semiconductor wafer with sign and dimension terminology for Hall contacts.

If the current polarity and magnetic field orientation are indexed as $I^{\pm}$ and $B^{\pm}$, and the potential measured across the Hall contacts is $V(B^{\pm},I^{\pm})$, the hall coefficient can be written as

$$R_H = \frac{2.5\times10^7 t}{|B|}\left[\frac{V(B^+I^+)}{I^+} + \frac{V(B^+I^-)}{I^-} - \frac{V(B^-I^+)}{I^+} + \frac{V(B^-I^-)}{I^-}\right]$$

where t is the thickness of the sample measured in centimeters, B is in Tesla, V is in voltage, and I is in ampere.

3.3.2 Experimental Setup

The samples were mounted in the liquid nitrogen cooled cryostat shown in Figure 11, which was placed in the variable field of a Varian electromagnet. We used a Keithley 200 current source and a Keithley 2000 multimeter. I automated the experiment using LabVIEW software and a IEEE 488.2 interface card as shown as a block diagram in Figure 14. The sample temperature was varied from 77 to 300 K using liquid nitrogen and a Lake shore Cryotronics temperature controller.

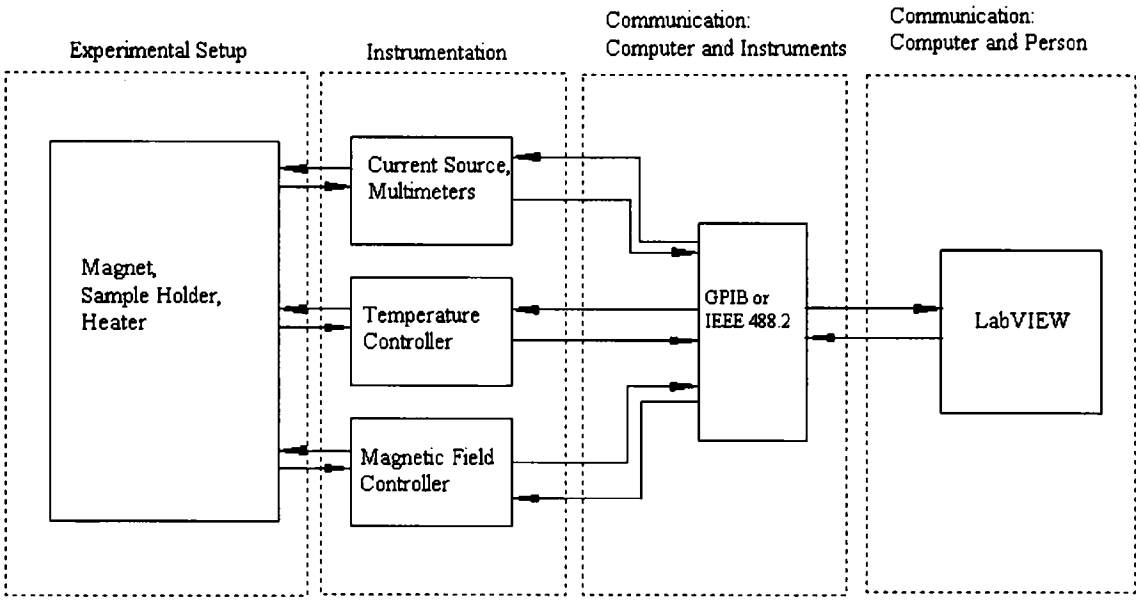

Figure 14. Block diagram of computer automation of Hall effect experiment.

CHAPTER IV

RESULTS AND DISCUSSIONS

4.1 Fourier Transform Infrared Spectroscopy

Figures 15 and 16 show the absorbance data taken for the samples with x=0.65 and 0.53 respectively. The data shown are taken at three different temperatures, indicating the change that occurs over the entire range measured. The interference fringes observed served to determine the layer thickness which was used to calculate the absorption coefficient, k.

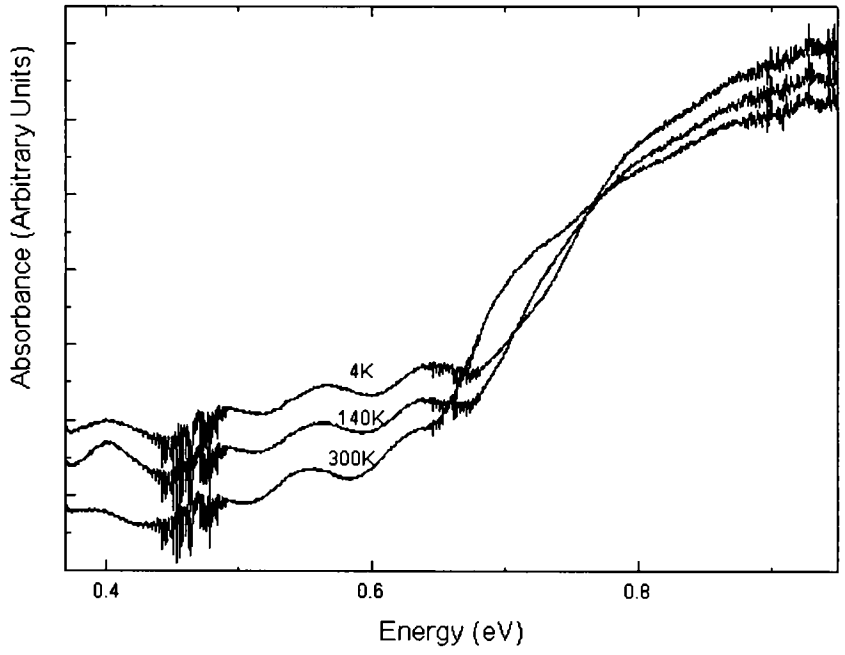

Figure 15. FTIR absorbance spectra obtained at T= 4, 140 and 300 K for a $GaAs_{0.35}Sb_{0.65}$ epilayer on a (001) - 8^0 toward (111)A GaAs substrate. Interference fringes are evident and were used to determine a layer thickness of 2.06μm. Water bands are apparent as noise in these spectra.

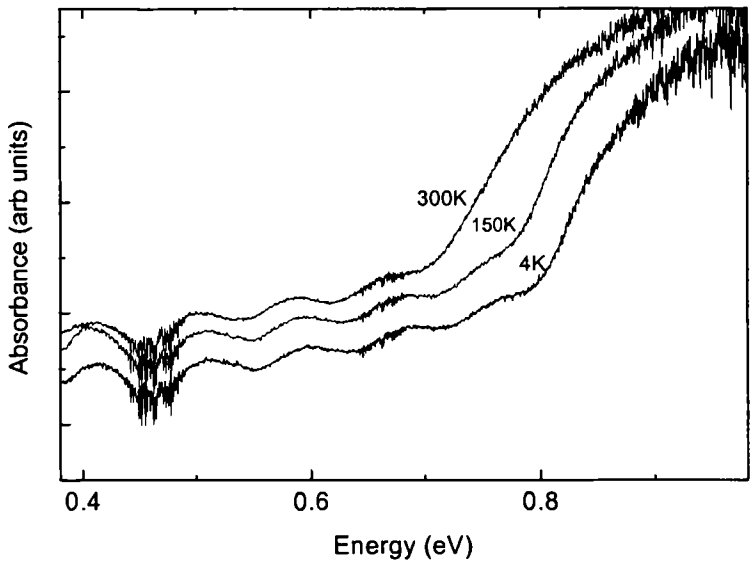

Figure 16. FTIR absorbance spectra obtained at T= 4, 150 and 300 K for a $GaAs_{0.47}Sb_{0.53}$ epilayer on a (115)B GaAs substrate. Interference fringes are evident and were used to determine a layer thickness of 1.92μm. Water bands are apparent as noise in these spectra.

The absorption coefficient squared was plotted as a function of photon energy for each temperature, an example of which is shown in Figure 17. Using the equation

$$k \propto (h\nu - E_g)^{1/2}$$

the energy gap, E_g, can be determined by linearly extrapolating from the band edge to the point where $k = 0$ as shown in Figure 18 for the sample x=0.65 at T=4 K.

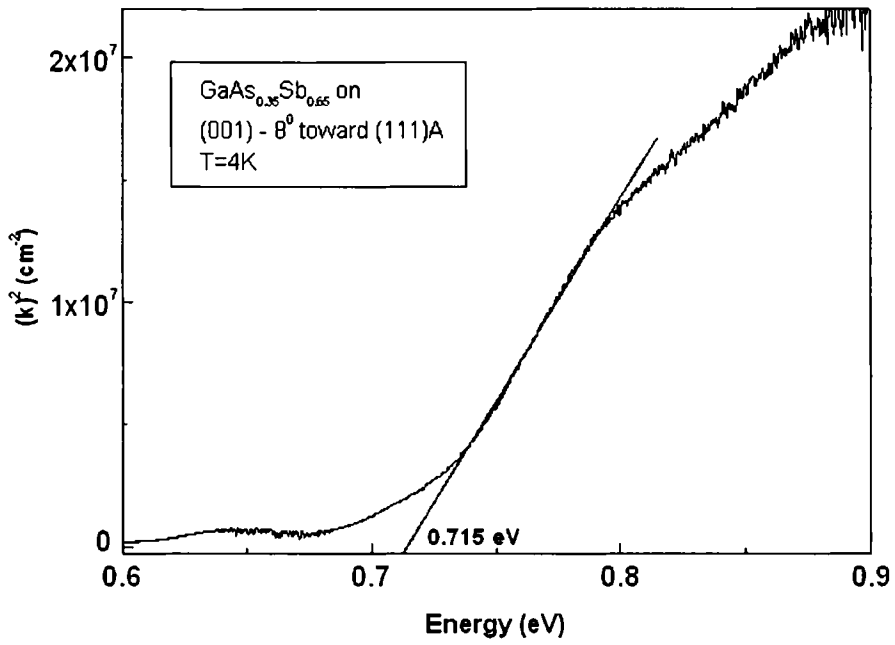

Figure 17. Absorption coefficient squared as a function of photon energy where E_g=0.715.

Finally, the energy gap at each temperature was plotted for the samples along with the best fit to the Varshni, O'Donnell, and Passler models, shown in Figure 18 for the

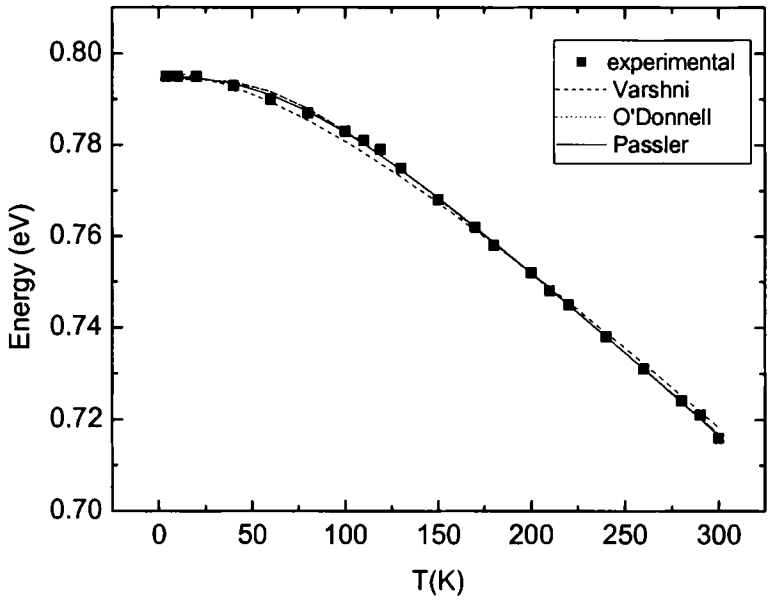

Figure 18. Temperature dependence of the energy gap for $GaAs_{0.47}Sb_{0.53}$ epilayer on a (115)B oriented GaAs substrate fitted by Varshni relation (dashed line), thermodynamic model by O'Donnell (dotted line) and Pässler model (solid line).

sample, x=0.53. While the Varshni and O'Donnell models give good fits, the Passler gives the best fit. The coefficients determined from each model are given in Table 2.

Model	Coefficient 1	Coefficient 2	Coefficient 3
Varshni	$\alpha = (4.2 \pm 0.1) \times 10^{-4}$ eV/K	$\beta = (189 \pm 9)$ K	—
O'Donnell and Chen	$S = 2.15 \pm 0.03$	$\langle \hbar\omega \rangle = (17.7 \pm 0.6)$ meV	—
Pässler and Oelgart	$\alpha = (3.7 \pm 0.1)$ meV/K	$\Theta = (195 \pm 18)$ K	$p = 2.5 \pm 0.2$

Table 2. Fitting parameters for the temperature dependence of the energy gap to the Varshni, O'Donnell and Chen, and Pässler and Oelgart models.

The differences between the predicted and measured values vary and are seen to lie between 30 and 50 meV. Similar discrepancy has been observed before for GaAsSb/InP epilayers [17], where the reduction in the energy gap was attributed to CuPt-B type ordering. This reduction is shown for the samples in Figure 19 where the solid line represents the predicted values for the random alloy based on the equation

$$E_g = 1.2x^2 - 1.9x + 1.43$$

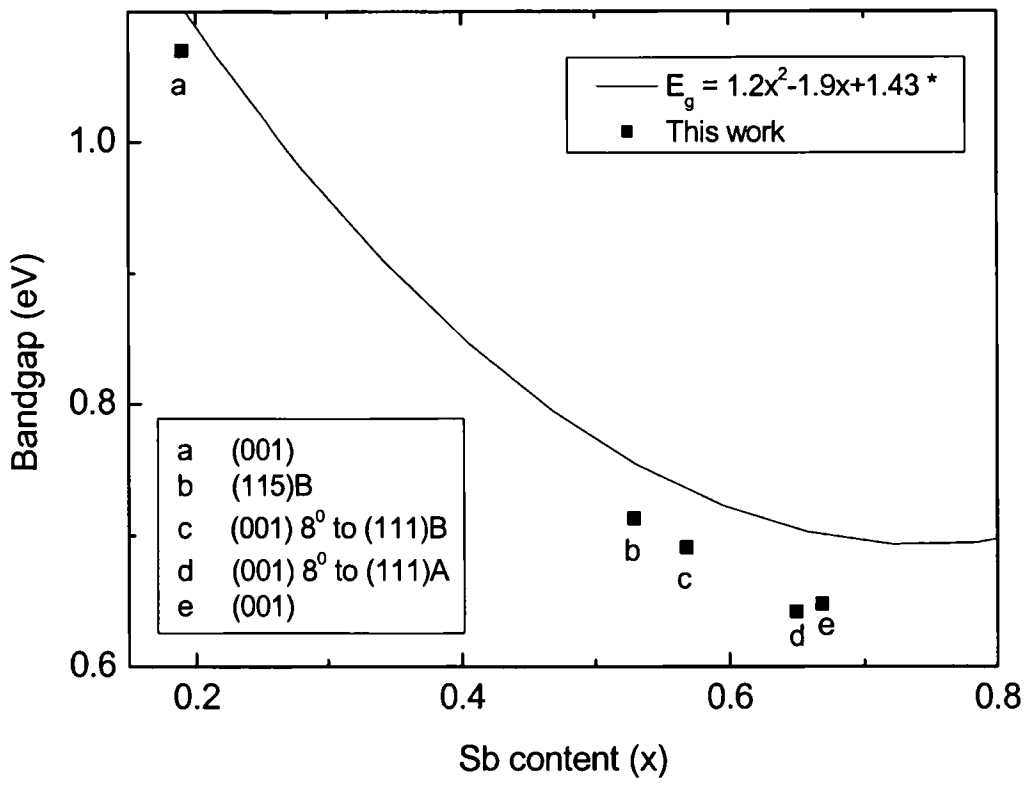

Figure 19. Room temperature energy gap versus composition for a series of $GaAs_{1-x}Sb_x$ epilayers. The results of this work are shown as solid squares. Sample 'a' exhibits quadruple period ordering [9], while samples 'b', 'c', 'd' and 'e' all exhibit CuPt-B type ordering.

This FTIR spectroscopy study determined the energy gap variance with temperature for several samples of ordered $GaAs_{1-x}Sb_x$ epilayers ($0.19 < x < 0.67$). We then used multiple published theoretical models and determined sets of coefficients for each model which best describe this temperature dependence. The resulting coefficients for each model can be applied generally to all published data for this alloy including compositions not included in our investigation. The presence of CuPt-B type atomic ordering was verified by TED measurements, and the resulting energy gap reduction could be used to estimate the degree of ordering in the samples investigated.

4.2 Hall Effect and Mobility

With the data from the optical work, I would like to further characterize the materials in the future using magneto-transport techniques. These techniques may include resistivity and Hall Effect using both high- and low-field magnets.

REFERENCES

[1] Shahidi G, Davari B, Taur Y, Warnock J, Wordeman M R, McFarland P, Mader S, Rodriquez M, Assenza R, Btonner G, Ginsberg B, Lii T, Polcari M and Ning T H 1990 IEDM Tech. Dig. **587**

[2] Omar M A 1975 Elementary Solid State Physics

[3] Kane E O 1966 Semiconductors and Semimetals **1** 75

[4] Zallen R "Handbook of Semiconductors" 1982 Vol 1 Chapter 1

[5] Lukic-Zrnic R, Gorman B P, Cottier R J, Littler C L, Golding T D and Norman A G 2002 Submitted to ICPS Conference

[6] Varshni Y P 1967 Physica **34** 149

[7] O'Donnell K P and Chen X 1991 Appl. Phys. Lett. **58** 2924

[8] Pässler R and Oelgart G 1997 J. Appl. Phys. **82** 2611

[9] Thurmond C D 1975 J. Electrochem. Soc. **122** 1133

[10] Pässler R 1996 Solid State Electron. **39** 1311

[11] Kittel C 1976 Introduction to Solid State Physics

[12] Norman A G, Seong T-Y, Philips B A, Booker G R and Mahajan S 1993 Presented at Microsc. Semecond. Mater. Conf.

[13] Yeo Y C, Li M F and Chong T C 1997 Phys. Rev. B **55** 16414

[14] Wei S H and Zunger A 1990 Appl. Phys. Lett **56** 662

[15] Laks D B, Wei S H and Zunger A 1992 Phys. Rev. Lett. **69** 3766

[16] Ploog K 1981 Ann. Rev. Mater. Sci. **11**

[17] Ihm Y E, Otsuka N, Klem J and Morkoc H 1987 Appl. Phys. Lett. **51** 2013